IEEE Access
Multidisciplinary | Rapid Review | Open Access Journal

Received May 8, 2020, accepted May 27, 2020, date of publication June 4, 2020, date of current version June 17, 2020.

Digital Object Identifier 10.1109/ACCESS.2020.3000042

Reconfigurable Multifunctional Metasurface for Broadband Polarization Conversion and Perfect Absorption

JIAYUN WANG[1], RONGCAO YANG[1,2], RUNBO MA[1], (Member, IEEE), JINPING TIAN[1], AND WENMEI ZHANG[1], (Member, IEEE)

[1]School of Physics and Electronic Engineering, Shanxi University, Taiyuan 030006, China
[2]Collaborative Innovation Center of Extreme Optics, Shanxi University, Taiyuan 030006, China

Corresponding author: Rongcao Yang (sxdxyrc@sxu.edu.cn)

This work was supported in part by the National Natural Science Foundation of China under Grant 61775126, in part by the Natural Science Foundation of Shanxi Province under Grant 201801D221164 and Grant 201801D121119, and in part by the Opened Fund of the State Key Laboratory of Integrated Optoelectronics under Grant IOSKL2019KF16.

ABSTRACT A reconfigurable multifunctional metasurface is proposed to realize the switching between broadband polarization conversion and perfect absorption by integrating the PIN diodes into the structure. An appropriate feed plate is designed to provide the bias voltage that controls the state of the diodes. When the diodes are in off-state, the metasurface will work in polarization conversion mode, which can convert the co-polarization wave into its cross-polarization state with polarization conversion ratio (PCR) of over 90% in the range from 2.97 to 6.03 GHz; While the diodes are in on-state, the metasurface exhibits perfect absorption with absorptivity of over 90% from 2.56 to 7.62 GHz, and the relative absorption bandwidth (RAB) reaches 99.4%. In addition, the metasurface is fabricated and measured to confirm the multifunctional performance. The proposed metasurface is expected to be applied in electromagnetic detection, stealth technology and communication system.

INDEX TERMS Reconfigurable metasurface, multifunction, broadband, polarization conversion, absorption.

I. INTRODUCTION

As 2-D version of artificial metamaterials, metasurfaces are the favored candidate for flexible manipulation of electromagnetic (EM) waves through artificially elegant design. They can be widely used in many applications, such as negative refraction [1], [2], lens [3], [4], light bending [5], polarization conversion [6]–[15], perfect absorption [16]–[25]. So far, some linear-to-linear [7]–[11], linear-to-circular [12], [13], and circular-to-circular [14], [15] polarization converters have been proposed, and at the same time, single band [16], [17], multi-band [18]–[21] and broadband perfect absorbers [22]–[25] have been studied. However, for most of these metasurfaces mentioned above, they only focused on the single function of polarization conversion or fixed-band absorption, which cannot meet the growing demands in complex circumstance.

The associate editor coordinating the review of this manuscript and approving it for publication was Vincenzo Conti.

Recently, many researchers are devoted to designing switchable or reconfigurable metasurfaces. In the THz band, some tunable materials such as graphene [26]–[28], photosensitive silicon [29], [30], and vanadium dioxide (VO_2) [31], [32], which can regulate the conductivity through chemical potential, pump power, or temperature, are often used to control the response of the metasurfaces to the EM waves. While in the microwave band, the controllable performances of the metasurfaces can be achieved by embedding fluid metals [33], [34], MEMS switches [35] or diodes [36]–[39] into the structures. Most recently, some multifunctional metasurfaces have been proposed based on the switchable and reconfigurable methods [40]–[44]. For example, Hong *et al.* incorporated VO_2 in the top-layer resonators and the bottom plate of the structure they designed to achieve reconfigurable transmission and reflection linear polarization conversion by controlling the temperature of VO_2 [40]; Liu *et al.* designed a galinstan-based metasurface to realize the conversion of linear polarization to cross polarization, circular polarization

and elliptical polarization by using microfluidic channels to control the working state of a L-shape resonator [41]. Cui *et al.* realized a multifunctional polarization converter by embedding varactors into the metasurface, which can convert incident linear polarization wave into different polarization modes by controlling the bias voltage of the varactors [42]. However, multifunctional metasurfaces with the performances of both polarization conversion and perfect absorption are rarely reported. In Ref. [43], Cao *et al.* designed a multifunctional metasurface structure that can realize polarization conversion and absorption in microwave frequency band, however, the structure is not controllable and its bandwidth of polarization conversion and absorption is relatively narrow. Therefore, reconfigurable multifunctional metasurfaces with broadband polarization conversion and perfect absorption are well worth studying.

In this paper, we firstly design a polarization converter and a perfect absorber, respectively. Then they are skillfully combined into a metasurface structure via incorporating PIN diodes in appropriate positions. By controlling the state of the PIN diodes, the metasurface can realize arbitrary switching between broadband polarization conversion and perfect absorption. When the PIN diodes are in off-state, the metasurface operates in polarization conversion mode with polarization conversion ratio (PCR) of above 90% in the range of 2.97 to 6.03 GHz; while the PIN diodes are in on-state, its operating mode will be switched to perfect absorption with absorptivity of above 90% from 2.56 to 7.62 GHz. Significantly, the operating bandwidth of the perfect absorption mode can completely cover the bandwidth of the polarization conversion mode, which ensures that all the EM energy in the target bandwidth cannot leak when the metasurface is operating in the perfect absorption mode. The proposed metasurface is distinctly different from the traditional switchable/tunable polarization converters [26], [29], [31], and it enriches the multifunctional metasurface family and has potential applications in EM detection, stealth technology, communication system and so on.

II. DESIGN PROCESSES AND SIMULATION RESULTS

A. REFLECTIVE BROADBAND POLARIZATION CONVERTER

Firstly, we design a reflective broadband linear polarization converter based on a fishbone-like resonator (FLR), as shown in Fig. 1(a). The unit cell of the converter is composed of a four-layer structure: the top layer is the FLR etched on the FR-4 dielectric substrate with a thickness of 1.6 mm, then an air spacer layer with a thickness of 8.5 mm is introduced between the FR-4 substrate and the metal ground plate, where the introduction of the air spacer layer can greatly reduce the usage of the dielectric substrate and lower the production cost. Both the FLR and the metal ground are copper with a thickness of 0.035 mm and the conductivity of 5.8×10^7S/m. The permittivity and the loss tangent of the FR-4 are $\varepsilon = 4.3$ and $tan\delta = 0.02$, respectively. In addition, the other

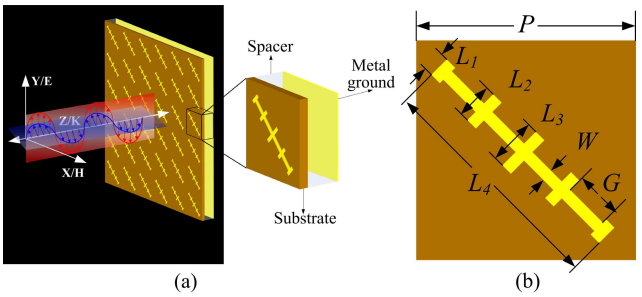

FIGURE 1. (a) Perspective view of the proposed metasurface. (b) Top view of the unit cell.

optimized parameters shown in Fig. 1(b) are as follows: $P = 24$ mm, $G = 4.5$ mm, $L_1 = 2.8$ mm, $L_2 = 3.8$ mm, $L_3 = 5.8$ mm, $L_4 = 23$ mm and $W = 1$ mm.

To demonstrate the performance of the proposed converter that can convert the incident co-polarization wave into a cross-polarization wave, we adopt the EM simulation software CST based on the finite integration technique (FIT) to model and simulate the structure. In the simulation, the unit cell boundary is set along the X-axis and the Y-axis, and an open (add space) boundary is set along the Z-axis, in which the electric field and magnetic field of the incident EM wave are polarized along the Y-axis and the X-axis, respectively, as shown in Fig. 1(a). The reflection coefficients of co-polarization and cross-polarization waves are defined as $r_{yy} = |E_{yr}|/|E_{yi}|$ and $r_{xy} = |E_{xr}|/|E_{yi}|$ [8], [10], respectively, where $|E_{yr}|$ and $|E_{yi}|$ are the reflected and incident electric field amplitudes along the Y-axis, respectively, so the polarization conversion rate (PCR) can be determined by $PCR = |r_{xy}|^2/\left(|r_{xy}|^2 + |r_{yy}|^2\right)$ [6].

As reported in previous articles [26], [31], the incident EM wave polarized along Y-axis can be decomposed into the two eigenmodes with clockwise and counterclockwise 45° (u-axis and v-axis direction) from the Y-axis direction, as shown in Fig. 2(a), they are the key factors to excite cross-polarization conversion. Thus, when the incident electric field is polarized along Y-axis direction, the incident and reflected electric field can be decomposed into $\vec{E}_i = \hat{u}E_{iu}e^{j\phi} + \hat{v}E_{iv}e^{j\phi}$ and $\vec{E}_r = \hat{u}r_uE_{iu}e^{j(\phi+\phi_u)} + \hat{v}r_vE_{iv}e^{j(\phi+\phi_v)}$, where E_{iu} and E_{iv} are the electric field components of the incident electric field along u-axis and v-axis, $r_u(r_v)$ and ϕ_u (ϕ_v) are the reflected amplitudes and phases, respectively. Due to the anisotropy of the converter structure, there is a phase difference $\Delta\varphi = \varphi_u - \varphi_v$. When the conditions of $r_u \approx r_v$ and $\Delta\varphi = 180°$ are satisfied simultaneously, one of E_{ru} and E_{rv} will be reversed, then the total electric field of the reflection wave will be converted to the X-direction, and the conversion of co-polarization wave to cross-polarization wave will be achieved. To confirm this, Fig. 2(b) shows the reflected amplitudes r_u and r_v, and the phase difference $\Delta\phi$ when the electric field of the incident EM wave is polarized along the u-axis and the v-axis, respectively. It can be seen from the Fig. 2(b) that r_u and r_v are approximately equal

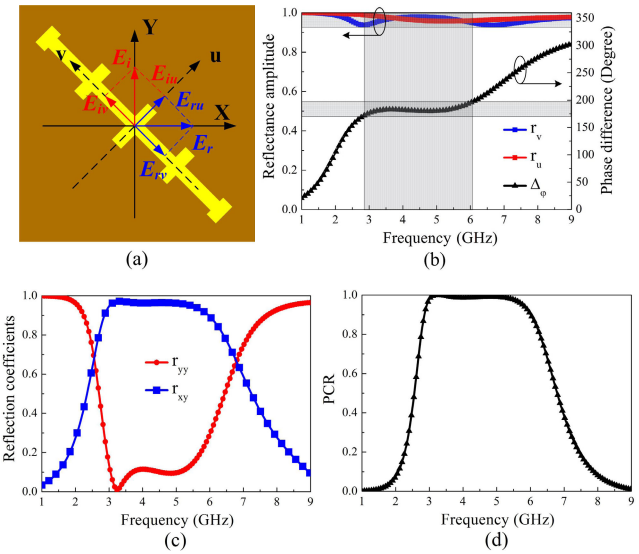

FIGURE 2. (a) Schematic illustration of the conversion from co-polarization to cross-polarization. (b) The reflection coefficients and the phase difference when the electric field is polarized along the u-axis and v-axis; Simulated (c) reflection coefficients and (d) the PCR of the polarization converter.

and the phase difference $\Delta\varphi$ is about 180° in the range from 2.85 to 6.01 GHz. This means that the converter has good polarization conversion performance in a broadband of about 3.16 GHz. Figs. 2(c) and (d) are the reflection coefficients and the PCR extracted from the simulation under normal incident. As can be seen from Figs. 2(c) and (d), in the range from 2.85 to 6.01 GHz, the co-polarization reflection coefficient is lower than 0.3, while the cross-polarization reflection coefficient is higher than 0.9, and the PCR reaches 90%. The relative conversion bandwidth is $W_{RCB} = 2(f_{\max} - f_{\min})/(f_{\max} + f_{\min}) = 71.3\%$, where the $f_{\max}$ and $f_{\min}$ are the maximum and minimum frequencies at the PCR of lager than 90%, respectively.

It is noted in Fig. 2(c) that there are two obvious resonant peaks at about 3.23 GHz and 4.82 GHz, where the PCR is close to 100%. The physical mechanism of the converter can be explained by the surface current distributions at these two frequencies, which are shown in Figs. 3(a) and (b). It can be clearly seen that at 3.23 GHz and 4.82 GHz, when the EM wave with the electric field polarized along the Y-axis is incident to the surface of the converter, a pair of anti-parallel currents are generated on the front FLR and the back metal ground, which will excite a dipolar oscillation m, then an induced magnetic field H is excited. Since the component H_y of the induced magnetic field H is parallel to the electric field component E_i of the incident EM wave, the cross coupling will occur between H_y and E_i, which will achieve the polarization conversion from co-polarization wave to cross-polarization wave. As the component H_x of the induced magnetic field H is parallel to the incident magnetic field component H_i, it cannot generate cross-polarization wave, but can promote the polarization conversion by weakening the H_i with the opposite direction [9], [31].

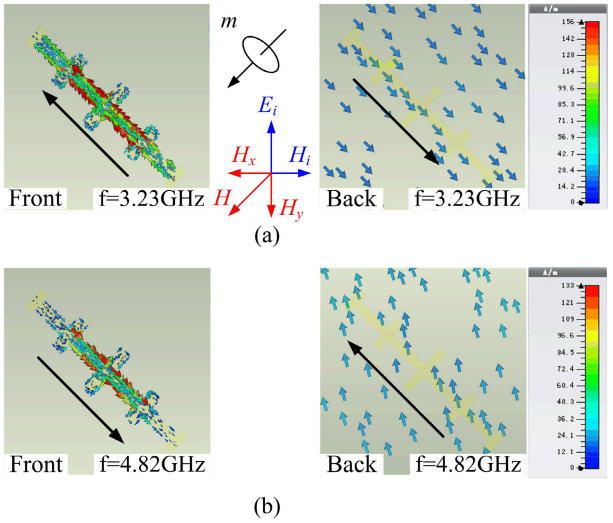

FIGURE 3. Surface current distributions of the front FLR and back metal ground at (a) 3.23 GHz and (b) 4.82 GHz, respectively.

B. ACTIVE SWITCHABLE BROADBAND ABSORBER

Further, we design an active switchable broadband absorber, as shown in Fig. 4. The absorber structure is similar to the polarization converter proposed in Part A except that the ground plate in Part A is replaced by a double-sided copper clad FR-4 substrate 2 with a thickness of 0.8 mm. The unit cell dimension P, the thickness of the dielectric substrate 1 and the air spacer as well as all the material parameters are the same as those in the polarization converter, which ensures that the absorber can operate in a similar bandwidth with the above mentioned polarization converter. The absorber adopts a diamond-cross resonator (DCR) which is embedded by lumped resistors (marked by black squares) and PIN diodes (marked by red triangles) to realize switchable broadband absorption, as shown in Fig. 4(b). The lumped resistors are ERJ-2RKF1800X produced by Panasonic [45], and its resistance is $R_{loaded} = 180\ \Omega$; the PIN diodes are BA591 produced by NXP [46], which is equivalent to a small resistance of $R_{on} = 0.36\ \Omega$ in series with an inductance of $L_d = 2$ nH in on-state, or a large capacitance of $C_{off} = 0.65$ pF and a resistance of $R_{off} = 100$ kΩ in series with the inductance L_d in off-state. As shown in Fig. 4(a), the front side of the substrate 2 serves as metal ground to prevent the transmission

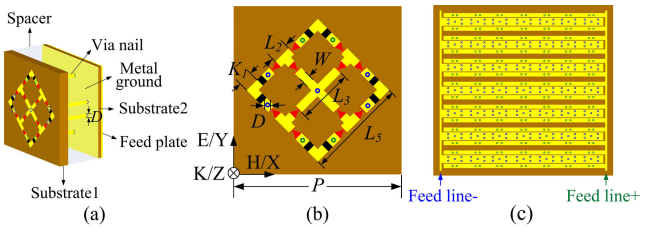

FIGURE 4. Schematic illustration of the broadband absorber (a) perspective view, (b) top view, (c) the bottom feed plate.

of EM waves, while its back side is used for the feeding plate to power the PIN diodes, as shown in Fig. 4(c). The anodes (marked by green circles) and cathodes (marked by blue circles) of the PIN diodes are respectively connected to the bottom feedlines through via nails with the length of 2.505 mm. In addition, the other structure parameters are as follows: $D = 0.6$ mm, $K_1 = 0.8$ mm, $W = 1$ mm, $L_2 = 3.8$ mm, $L_3 = 5.8$ mm and $L_5 = 13$ mm.

The proposed absorber is also modeled and simulated by the EM simulation software CST in the same simulation environment as in the Part A. The absorptivity can be defined as $A(\omega) = 1 - R(\omega) - T(\omega)$, where the $R(\omega)$ and $T(\omega)$ are the reflectivity and the transmissivity, respectively. The simulated reflection coefficients, transmission coefficients and the absorptivity are shown in Fig. 5. As the metal ground prevents the transmission of EM waves, the transmissivity is nearly zero, which is in agreement with the simulated results, see the dark yellow and violet lines of t_{yy} and t_{xy} in Figs. 5(a) and (b). Thus, it is only necessary to consider the reflection coefficients of co-polarization r_{yy} and cross-polarization r_{xy}, and the absorptivity can be calculated as $A(\omega) = 1 - |r_{yy}|^2 - |r_{xy}|^2$. It can be seen clearly from Fig. 5(a) that when the diodes are in on-state, the co-polarization reflection coefficient r_{yy} less than 0.3 in the range from 2.97 to 7.37 GHz, and the cross-polarization reflection coefficient r_{xy} is near zero, so the absorptivity is more than 90%, and the relative absorption bandwidth $W_{RAB} = 85.1\%$. While the diodes are in off-state, as shown in Fig. 5(b), the co-polarization EM waves incident to the absorber will be almost completely reflected, and the maximum absorptivity is only 10.2%.

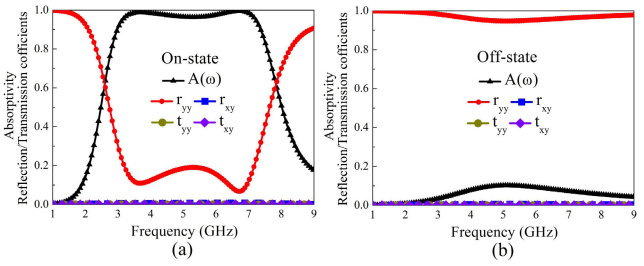

FIGURE 5. Simulated reflection and transmission coefficients as well as the absorptivity of the DCR when the PIN diodes are in (a) on-state and (b) off-state.

The absorption mechanism of the absorber can be analyzed by the impedance match theory and the surface current distributions. According to impedance match theory, when the equivalent impedance of the absorber matches to the impedance in free space, *i. e.* $Z(\omega) = \sqrt{\mu(\omega)/\varepsilon(\omega)} \approx Z_0$, the EM wave will enter the absorber almost completely, and then the EM energy will be dissipated by the ohmic loss and dielectric loss inside the absorber. Fig. 6 presents the normalized complex impedance of the absorber as a function of frequency when the diodes are in on-state and off-state. It can be seen from Fig. 6(a) that when the diodes are in on-state, the imaginary part of the impedance is very small and

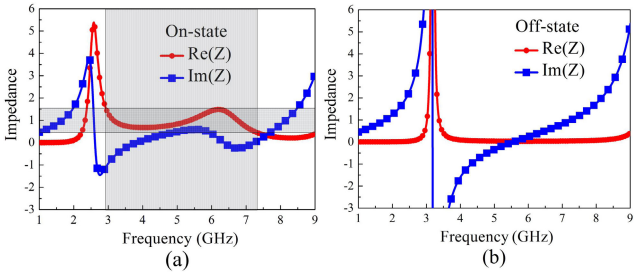

FIGURE 6. Normalized complex impedance of the DCR when the diodes are in (a) on-state and (b) off-state, respectively.

the real part is close to 1 in the band from 2.97 to 7.37 GHz, which indicates that the equivalent impedance of the absorber can match to the impedance in the free space, thus the proposed absorber exhibits a good absorption performance. While the diodes are in off-state, as shown in Fig. 6(b), the impedance matching condition is broken, so the absorption peak is turned off. Furthermore, Fig. 7 depicts the surface current distributions at the resonant frequencies of 3.63 GHz and 6.71 GHz. When the diodes are in on-state, the diamond ring and cross are interconnected, and the DCR can be considered as a whole to respond to the incident EM wave, exhibiting a magnetic response. As shown in Fig. 7(a), a pair of anti-parallel currents is formed on the DCR and the back ground plate. However, when the diodes are in off-state, the DCR is equivalently cut apart into several small parts, the strong magnetic response between the DCR and the back ground plate disappears, thus the surface currents are very weak, as shown in Fig. 7(b), and the EM wave will be almost completely reflected. Therefore, by changing the state of the diodes, the controllable broadband absorption can be realized.

Additionally, we investigate the absorption performance of the DCR absorber at different polarization angles and different incident angles. Since the DCR is quadruple rotational symmetry, the absorber is insensitive to the polarization angles. Fig. 8(a) is the absorptivity at different polarization angles under normal incidence, from which can be seen that the absorption performance is hardly affected by the polarization angles. Figs. 8(b) and (c) are the absorptivity at different incident angles for TE and TM polarization modes, respectively. It is observed from Figs. 8(b) and (c) that when the incident angle increases to 50°, the absorber still has good absorption performance for both TE and TM polarization modes. It is noticed that in the range from 8 to 9 GHz, an additional absorption peak appears with the increasing of the incident angles, which might arise from the higher order resonant modes [19], [20] and the mismatched impedance under oblique incidence [23].

C. RECONFIGURABLE BROADBAND POLARIZATION CONVERTER/ABSORBER

Although both the broadband polarization converter presented in Part A and the broadband switchable absorber demonstrated in Part B have good performances, they can

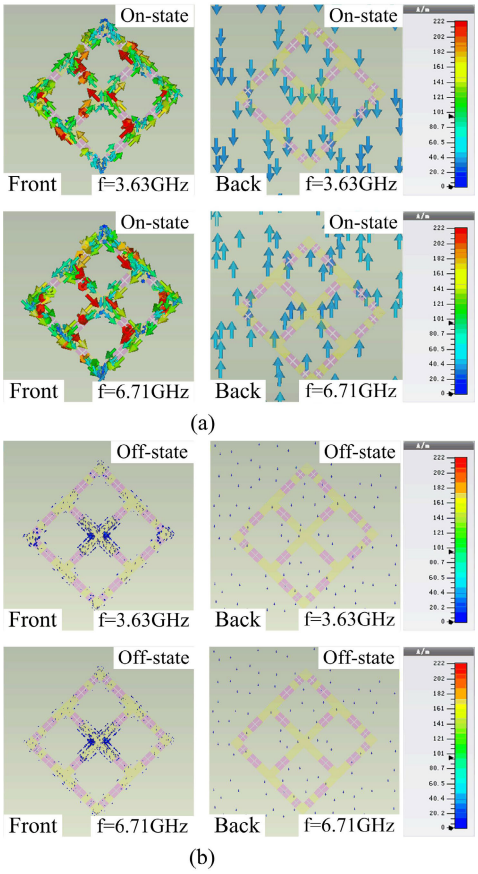

FIGURE 7. Surface current distributions on the DCR and the metal ground at 3.63 GHz and 6.71 GHz when the diodes are in (a) on-state and (b) off-state, respectively.

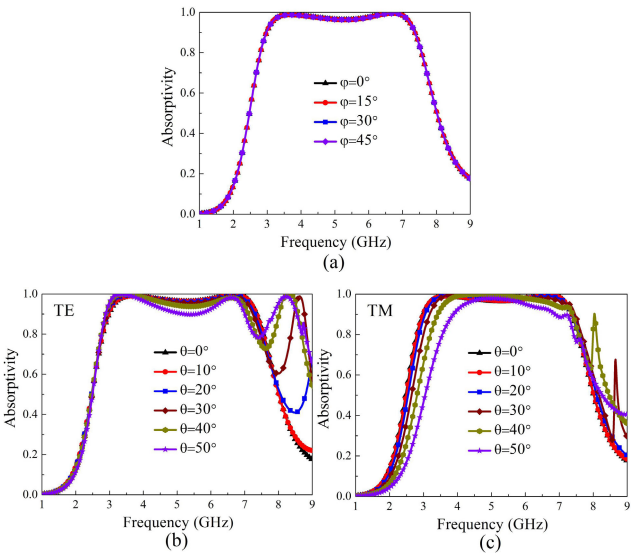

FIGURE 8. (a) Absorptivity of the DCR under different polarization angles for normal incidence; absorptivity under different incident angles for (b) TE and (c) TM polarized incident wave, respectively.

only operate in a single function mode. In order to achieve a reconfigurable multifunctional broadband polarization converter/absorber, we skillfully combine the FLR in Part A and the DCR in Part B to form a FL-DCR through optimizing the resonator structure, as shown in Fig. 9. Here the thickness of the air spacer and the substrate, the lumped resistors, the PIN diodes, and the material parameters are the same as those in Part B. The additional structural parameters are $K_2 = 6.1$ mm and $K_3 = 1.5$ mm, and the other parameters are identical to those in Part A and Part B. When the diodes are in on-state, the structure can be regarded as quadruple rotational symmetry that can absorb EM waves with arbitrary polarization angles; while the diodes are in off-state, the FL-DCR will behave as a diagonally symmetrical structure which can realize the conversion from co-polarization wave to cross-polarization wave [7], [8]. In order to realize the switch between the polarization converter and the absorber, the bottom feed plate is updated, as shown in Fig. 9(c), and the corresponding structural parameters are as follow: $L_6 = 174$ mm, $g_1 = 2$ mm, $g_2 = 1$ mm, $g_3 = 45°$. The anodes (marked by green circles) and cathodes (marked by blue circles) of the PIN diodes and the bottom feedlines are marked in Fig. 9(b) and (c).

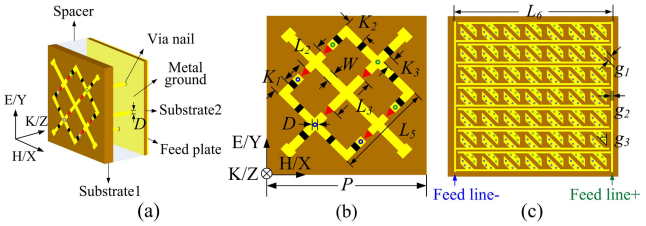

FIGURE 9. Schematic illustration of the converter/absorber (a) perspective view, (b) top view, (c) the bottom feed plate.

The multifunctional converter/absorber is simulated under the same simulation environment as mentioned above, and the results are shown in Fig. 10. It can be seen from Fig. 10(a) that when the diodes are in off-state, it operates in polarization conversion mode, the PCR is more than 90% in the range of 2.97 to 6.03 GHz, and $W_{RCB} = 68\%$; while the diodes are in on-state, the FLR and DCR are electrically connected, the EM waves can be absorbed almost entirely due to the high loss of the lumped resistors, and the absorptivity is larger than 90% from 2.56 to 7.62 GHz with $W_{RAB} = 99.4\%$, as shown in Fig. 10(b).

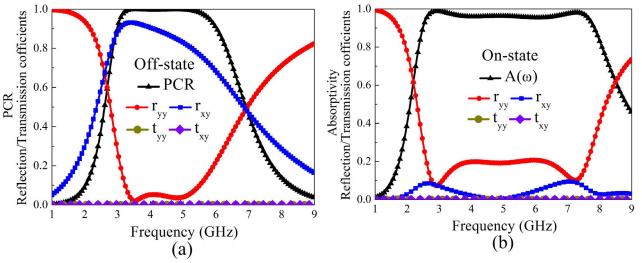

FIGURE 10. (a) Polarization conversion performance when the diodes are in off-state and (b) absorption performance when the diodes are in on-state.

Figs. 11 and 12 depict the surface current distributions and magnetic field distributions at the resonant frequencies

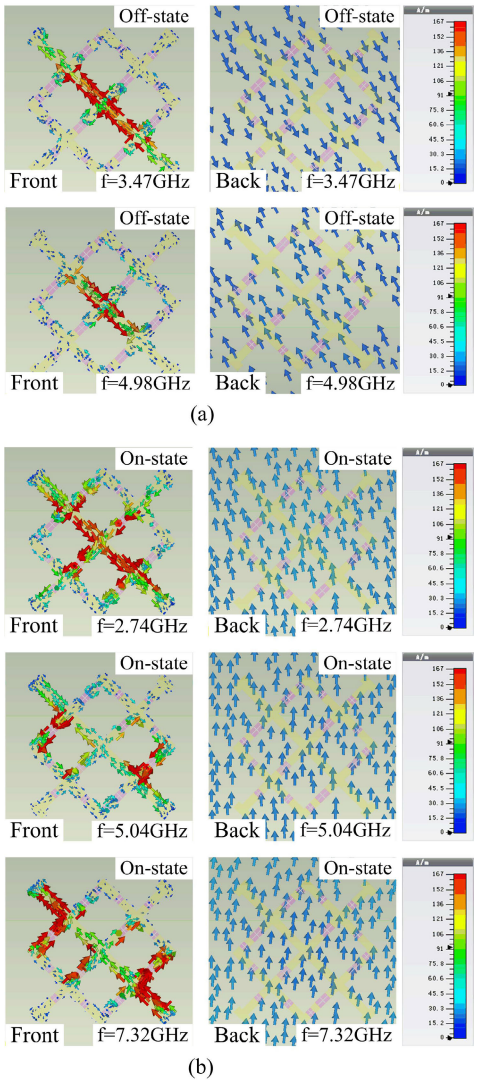

FIGURE 11. Surface current distributions of the front FL-DCR and the metal ground when (a) the diodes are in off-state at 3.47 GHz and 4.98 GHz and (b) the diodes are in on-state at 2.74 GHz, 5.04 GHz and 7.32 GHz, respectively.

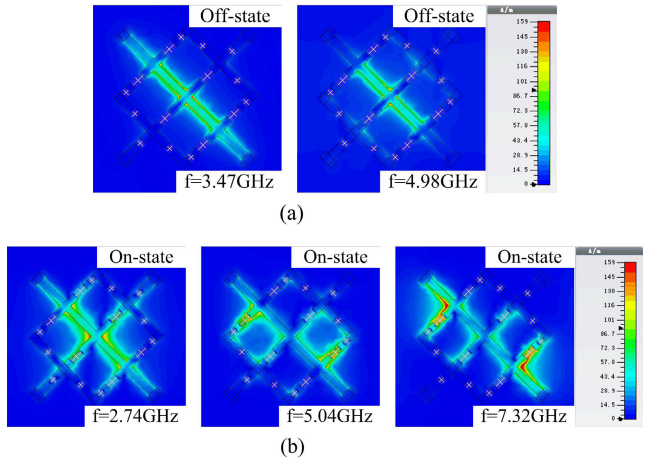

FIGURE 12. Magnetic field distributions of the FL-DCR for (a) the diodes in off-state at 3.47 GHz and 4.98 GHz, (b) the diodes in on-state at 2.74 GHz, 5.04 GHz and 7.32 GHz, respectively.

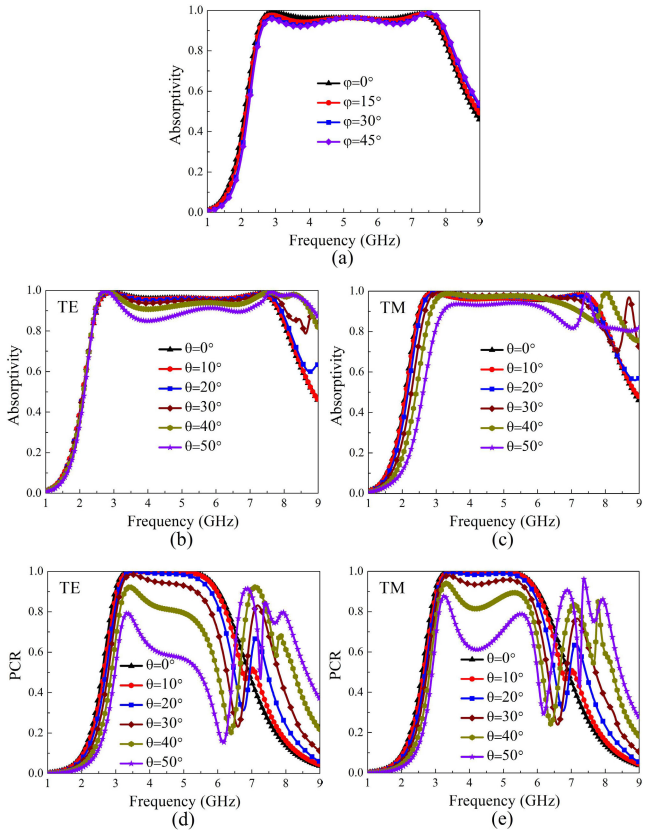

FIGURE 13. (a) Absorptivity of the FL-DCR under different polarization angles under normal incidence; (b), (c) absorptivity and (d), (e) PCR under different incident angles for TE and TM polarized incident wave, respectively.

when the diodes are in different states. It can be observed from Figs. 11(a) and 12(a) that when the diodes are in off-state, the surface currents and magnetic field are mainly distributed on the FLR, which means that the FLR dominates the polarization conversion function. Similar to the case in Part A, the surface currents distributed on the FL-DCR and the back metal ground are anti-parallel, which will excite the magnetic dipole resonance. This will result in the conversion of co-polarization wave to cross-polarization wave. When the diodes are in on-state, the surface currents and magnetic field are distributed on different positions of the FL-DCR at different resonance frequencies, as shown in Figs. 11(b) and 12(b). It is clear that the surface currents and magnetic field are distributed on the middle cross part, the two diagonal parts of the DCR, and the corners of the junctions of the FLR and the DCR at 2.74 GHz, 5.04 GHz and 7.32 GHz, respectively. This implies that the resonances at the three different frequencies and the high loss of the lumped resistors contribute to the broadband absorption.

Furthermore, we discuss the polarization conversion and absorption performance of the FL-DCR under different polarization angles and incident angles of the incident EM waves. Fig. 13(a) is the absorptivity at different polarization angles

under normal incident when the diodes are in on-state. It can be seen from Fig. 13(a) that when the polarization angle changes from 0° to 45°, the absorptivity is hardly affected because the FL-DCR structure is approximately quadruple rotational symmetric when the diodes are in on-state. Figs. 13(b) and (c), 13(d) and (e) are the absorptivity and the PCR under different incident angles, respectively. For both TE and TM waves, the good absorptivity can be maintained when the incident angle increases to 50°, while the good polarization conversion performance is remained when the incident angle is less than 30°. In addition, it is noted that the absorptivity and PCR for TE wave decrease faster in the middle of absorption band with the increasing of the incident angle. It is because the magnetic field of the TE wave cannot efficiently drive anti-parallel currents between the front resonator and the back metal ground under oblique incident angles [17]. Moreover, the deterioration of PCR is also observed from Figs. 13(d)-(e) with the increasing of incident angles. According to Formulas (1) and (2) in Ref. [8], the propagation phase in the dielectric spacer for oblique incidence can be denoted as $2\beta = 2\sqrt{\varepsilon}k_0 t/\cos\theta_t$ which is greater than $2\sqrt{\varepsilon}k_0 t$ under normal incidence, where k_0 is the wave vector in free space, t is the thickness of the dielectric and θ_t is the angle of refraction in the dielectric. The additional propagation phase will destroy the interference condition at the top surface of the absorber, and will further affect the value of r_{xy}. Especially, at higher frequency, the additional propagation phase changes more drastically when the incident angle θ is increased, which will cause the deterioration of PCR at higher frequency.

III. FABRICATION AND MEASURMENT

We fabricated a prototype of the FL-DCR broadband polarization converter/absorber by using circuit board etching technique, as shown in Figs. 14(a-c), where the geometrical dimensions and the material parameters of the fabricated prototype are the same as those in the simulation. Fig. 14(a) is the top view of the prototype, 7×7 unit cells of the FL-DCR are etched on the front of the dielectric substrate 1, the PIN diodes BA591 are welded at the junctions of the FLR and DCR, and the lumped resistors ERJ-2RKF1800X are embedded at the appropriate position of the DCR, the anodes and cathodes of the PIN diodes are respectively connected to the feedline+ and feedline− on the back of the substrate 2 through via nails, as shown in Fig. 14(b). In addition, the substrate 1 and substrate 2 are fixed with plastic nuts at the four corners of the prototype to form an air spacer with the thickness of 9 mm, as shown in Fig. 14(c).

In experiment, we adopt an approximate NRL arch method [21], [47] to measure the prototype in the free space, as shown in Fig. 14(d). The transmitting and receiving horns (H1 and H2) are connected to the vector network analyzer (Agilent N5222A) through a low loss coaxial cable, respectively, the distance between the horn antennas and the prototype meets the far-field conditions of the NRL standard, a DC stabilized power supply (SS2323) is applied to provide

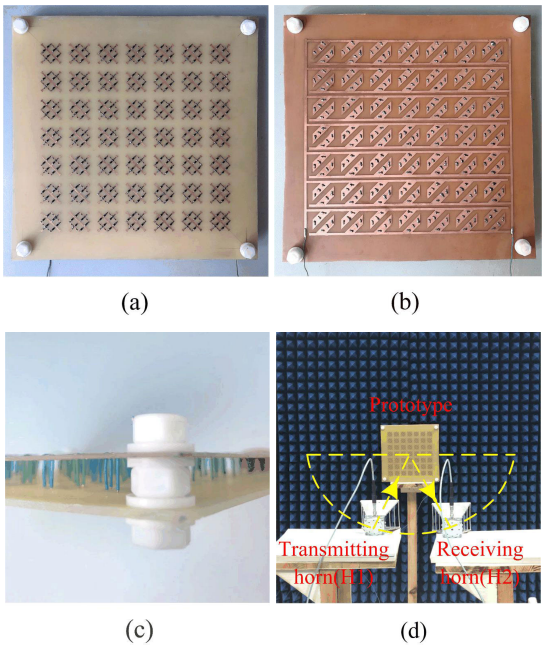

FIGURE 14. Photos of fabricated prototype for (a) top view, (b) bottom view and (c) side view, and (d) photo of measurement setup.

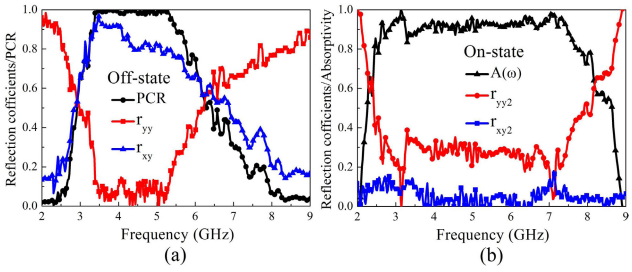

FIGURE 15. Measured results of the broadband polarization converter/absorber. (a) polarization conversion performance for the diodes in off-state, (b) absorption performance for the diodes in on-state.

bias voltage for the PIN diodes, the wedge foam materials are placed behind the prototype to eliminate the interference from scattering and unnecessary reflection.

Firstly, we measured the reflection coefficients in the polarization conversion mode by applying the reverse bias voltage 21 V on the prototype, *i. e.* the PIN diodes are in off-state, H1 and H2 are horizontally placed to transmit and receive the horizontally polarized waves, respectively, so the co-polarized reflection wave is received. Then, we kept the positions of H1 and H2 invariant, and rotated the H2 by 90° to receive the cross-polarized reflection wave. Before each measurement, we calibrated the equipments by using a metal plate with the same size as the prototype [42]. The measured reflection coefficients of co-polarization and cross-polarization waves and the PCR are shown in Fig. 15(a). It can be seen that the PCR is more than 90% in the range of 3.33 to 5.48 GHz. Similarly, we set the PIN diodes to on-state by applying the forward bias voltage of 2.0 V, the co-polarized and cross-polarized reflection coefficients in the

absorption mode are measured by the same method, as shown in Fig. 15(b). It can be seen from Fig. 15(b) that the absorptivity is over 90% from 2.63 to 7.51 GHz. Compared with the simulated results in Fig. 10, it can be found that the measured results are in good agreement with the simulated ones except that the bandwidth of the test results is slightly reduced, which might arise from manufacturing and measurement errors such as the errors of two calibrations by mechanical rotation of the H2.

IV. CONCLUSION

In this paper, we reported a reconfigurable multifunctional metasurface that combines a FLR polarization converter and a DCR absorber through the PIN diodes. The metasurface can achieve the arbitrary switching between broadband polarization conversion and perfect absorption. When the diodes are in off-state, the proposed metasurface can convert the incident co-polarization wave to cross-polarization wave with the PCR of above 90% in the range of 2.97 to 6.03 GHz; while the diodes are in on-state, the incident wave will be absorbed almost entirely with $W_{RAB} = 99.4\%$ in the band from 2.56 to 7.62 GHz. It is noteworthy that the operating bandwidth in the perfect absorption mode can completely cover the bandwidth in the polarization conversion mode, which ensures the seal of EM energy in the target band. The physical mechanism of the proposed metasurface is explained by the surface current and magnetic field distributions at the resonance frequencies. In addition, the proposed structure has almost polarization insensitivity in the absorption mode, and it shows good insensitivity to the incident EM wave under certain incident angles in the polarization conversion and perfect absorption mode. Finally, we fabricated a prototype of the multifunctional metasurface, and measured it in the free space. The measured results and simulated results are in good agreement. This research provides a simple and effective method for realizing reconfigurable multifunctional metasurface, which is expected to be applied in EM detection, stealth technology, communication system and so on.

REFERENCES

[1] R. A. Shelby, D. R. Smith, S. C. Nemat-Nasser, and S. Schultz, "Microwave transmission through a two-dimensional, isotropic, left-handed metamaterial," *Appl. Phys. Lett.*, vol. 78, no. 4, pp. 489–491, Jan. 2001.

[2] D. R. Smith, J. B. Pendry, and M. C. K. Wiltshire, "Metamaterials and negative refractive index," *Science*, vol. 305, no. 5685, pp. 788–792, Aug. 2004.

[3] L. Huang, X. Chen, H. Mühlenbernd, H. Zhang, S. Chen, B. Bai, Q. Tan, G. Jin, K.-W. Cheah, C.-W. Qiu, J. Li, T. Zentgraf, and S. Zhang, "Three-dimensional optical holography using a plasmonic metasurface," *Nature Commun.*, vol. 4, no. 1, p. 2808, Nov. 2013.

[4] F. Aieta, P. Genevet, M. A. Kats, N. Yu, R. Blanchard, Z. Gaburro, and F. Capasso, "Aberration-free ultrathin flat lenses and axicons at telecom wavelengths based on plasmonic metasurfaces," *Nano Lett.*, vol. 12, no. 9, pp. 4932–4936, Aug. 2012.

[5] X. Ni, N. K. Emani, A. V. Kildishev, A. Boltasseva, and V. M. Shalaev, "Broadband light bending with plasmonic nanoantennas," *Science*, vol. 335, no. 6067, p. 427, Jan. 2012.

[6] J. Hao, Y. Yuan, L. Ran, T. Jiang, J. A. Kong, C. T. Chan, and L. Zhou, "Manipulating electromagnetic wave polarizations by anisotropic metamaterials," *Phys. Rev. Lett.*, vol. 99, no. 6, Aug. 2007, Art. no. 063908.

[7] N. K. Grady, J. E. Heyes, D. R. Chowdhury, Y. Zeng, M. T. Reiten, A. K. Azad, A. J. Taylor, D. A. R. Dalvit, and H.-T. Chen, "Terahertz metamaterials for linear polarization conversion and anomalous refraction," *Science*, vol. 340, no. 6138, pp. 1304–1307, Jun. 2013.

[8] X. Gao, X. Han, W.-P. Cao, H. O. Li, H. F. Ma, and T. J. Cui, "Ultrawideband and high-efficiency linear polarization converter based on double V-Shaped metasurface," *IEEE Trans. Antennas Propag.*, vol. 63, no. 8, pp. 3522–3530, Aug. 2015.

[9] J. Zhu, S. Li, L. Deng, C. Zhang, Y. Yang, and H. Zhu, "Broadband tunable terahertz polarization converter based on a sinusoidally-slotted graphene metamaterial," *Opt. Mater. Express*, vol. 8, no. 5, pp. 1164–1173, May 2018.

[10] F. Li, H. Chen, L. Zhang, Y. Zhou, J. Xie, L. Deng, and V. G. Harris, "Compact high-efficiency broadband metamaterial polarizing reflector at microwave frequencies," *IEEE Trans. Microw. Theory Techn.*, vol. 67, no. 2, pp. 606–614, Feb. 2019.

[11] M. Yan, J. Wang, Y. Pang, C. Xu, H. Chen, L. Zheng, J. Zhang, and S. Qu, "An FSS-backed dual-band reflective polarization conversion metasurface," *IEEE Access*, vol. 7, pp. 104435–104442, 2019.

[12] X. Wu, Y. Meng, L. Wang, J. Tian, S. Dai, and W. Wen, "Anisotropic metasurface with near-unity circular polarization conversion," *Appl. Phys. Lett.*, vol. 108, no. 18, May 2016, Art. no. 183502.

[13] Y. N. Jiang, L. Wang, J. Wang, C. N. Akwuruoha, and W. P. Cao, "Ultra-wideband high-efficiency reflective linear-to-circular polarization converter based on metasurface at terahertz frequencies," *Opt. Express*, vol. 25, no. 22, pp. 27616–27623, Oct. 2017.

[14] X. Ma, C. Huang, M. Pu, C. Hu, Q. Feng, and X. Luo, "Multi-band circular polarizer using planar spiral metamaterial structure," *Opt. Express*, vol. 20, no. 14, pp. 16050–16058, Jun. 2012.

[15] S.-Y. Wang, W. Liu, and W. Geyi, "A circular polarization converter based on in-linked loop antenna frequency selective surface," *Appl. Phys. B, Lasers Opt.*, vol. 124, no. 6, p. 126, Jun. 2018.

[16] N. I. Landy, S. Sajuyigbe, J. J. Mock, D. R. Smith, and W. J. Padilla, "Perfect metamaterial absorber," *Phys. Rev. Lett.*, vol. 100, May 2008, Art. no. 207402.

[17] H. Tao, C. M. Bingham, A. C. Strikwerda, D. Pilon, D. Shrekenhamer, N. I. Landy, K. Fan, X. Zhang, W. J. Padilla, and R. D. Averitt, "Highly flexible wide angle of incidence terahertz metamaterial absorber: Design, fabrication, and characterization," *Phys. Rev. B, Condens. Matter*, vol. 78, no. 24, Dec. 2008, Art. no. 241103.

[18] H. Li, L. H. Yuan, B. Zhou, X. P. Shen, Q. Cheng, and T. J. Cui, "Ultrathin multiband gigahertz metamaterial absorbers," *J. Appl. Phys.*, vol. 110, no. 1, Jul. 2011, Art. no. 014909.

[19] X. Shen, Y. Yang, Y. Zang, J. Gu, J. Han, W. Zhang, and T. J. Cui, "Triple-band terahertz metamaterial absorber: Design, experiment, and physical interpretation," *Appl. Phys. Lett.*, vol. 101, no. 15, Oct. 2012, Art. no. 154102.

[20] G. D. Wang, J. F. Chen, X. W. Hu, Z. Q. Chen, and M. H. Liu, "Polarization-insensitive triple-band microwave metamaterial absorber based on rotated square rings," *Prog. Electromagn. Res.*, vol. 145, pp. 175–183, Mar. 2014.

[21] J. Y. Wang, R. C. Yang, J. P. Tian, X. W. Chen, and W. M. Zhang, "A dual-band absorber with wide-angle and polarization insensitivity," *IEEE Antennas Wireless Propag. Lett.*, vol. 17, no. 7, pp. 1242–1246, Jul. 2018.

[22] T. Jang, H. Youn, Y. J. Shin, and L. J. Guo, "Transparent and flexible polarization-independent microwave broadband absorber," *ACS Photon.*, vol. 1, no. 3, pp. 279–284, Feb. 2014.

[23] C. Zhang, Q. Cheng, J. Yang, J. Zhao, and T. J. Cui, "Broadband metamaterial for optical transparency and microwave absorption," *Appl. Phys. Lett.*, vol. 110, no. 14, Apr. 2017, Art. no. 143511.

[24] T. T. Nguyen and S. Lim, "Angle- and polarization-insensitive broadband metamaterial absorber using resistive fan-shaped resonators," *Appl. Phys. Lett.*, vol. 112, no. 2, Jan. 2018, Art. no. 021605.

[25] Q. Yuan, S. Qu, H. Ma, S. Sui, Y. Shen, J. Wang, M. Feng, H. Chen, Y. Jin, and X. Wang, "A broadband wide-angle synthetical absorber designed by topology optimization of resistance surface and metal wires," *IEEE Access*, vol. 7, pp. 142675–142681, 2019.

[26] C. Yang, Y. Luo, J. X. Guo, Y. Pu, D. He, Y. D. Jiang, J. Xu, and Z. J. Liu, "Wideband tunable mid-infrared cross polarization converter using rectangle-shape perforated graphene," *Opt. Express*, vol. 24, no. 15, pp. 16913–16922, Jul. 2016.

[27] Y. T. Zhao, B. Wu, B. J. Huang, and Q. Cheng, "Switchable broadband terahertz absorber/reflector enabled by hybrid graphene-gold metasurface," *Opt. Express*, vol. 25, no. 7, pp. 7161–7169, Apr. 2017.
[28] S. J. Kindness, N. W. Almond, W. Michailow, B. B. Wei, L. A. Jakob, K. Delfanazari, P. B. Weimer, S. Hofmann, H. E. Beere, D. A. Ritchie, and R. Degl'Innocenti, "Graphene integrated metamaterial device for all electrical polarization control of terahertz quantum cascade lasers," *ACS Photon.*, vol. 6, pp. 1547–1555, May 2019.
[29] J. C. Zhao, Y. Z. Cheng, and Z. Z. Cheng, "Design of a photo-excited switchable broadband reflective linear polarization conversion metasurface for terahertz waves," *IEEE Photon. J.*, vol. 10, no. 1, Feb. 2018, Art. no. 4600210.
[30] S. Yuan, R. Yang, J. Xu, J. Wang, and J. Tian, "Photoexcited switchable single-/dual-band terahertz metamaterial absorber," *Mater. Res. Express*, vol. 6, no. 7, Apr. 2019, Art. no. 075807.
[31] X. Zheng, Z. Xiao, and X. Ling, "A tunable hybrid metamaterial reflective polarization converter based on vanadium oxide film," *Plasmonics*, vol. 13, no. 1, pp. 287–291, Jan. 2017.
[32] H.-E. Su, J.-L. Li, and L. Xia, "A novel temperature controlled broadband metamaterial absorber for THz applications," *IEEE Access*, vol. 7, pp. 161255–161263, 2019.
[33] K. Ling, H. Kim, M. Yoo, and S. Lim, "Frequency-switchable metamaterial absorber injecting eutectic gallium-indium (EGaIn) liquid metal alloy," *Sensors*, vol. 15, no. 11, pp. 28154–28165, Nov. 2015.
[34] H. K. Kim, D. Lee, and S. Lim, "Wideband-switchable metamaterial absorber using injected liquid metal," *Sci. Rep.*, vol. 6, no. 1, p. 31823, Aug. 2016.
[35] P. Pitchappa, C. Pei Ho, P. Kropelnicki, N. Singh, D.-L. Kwong, and C. Lee, "Micro-electro-mechanically switchable near infrared complementary metamaterial absorber," *Appl. Phys. Lett.*, vol. 104, no. 20, May 2014, Art. no. 201114.
[36] B. Zhu, Y. Feng, J. Zhao, C. Huang, and T. Jiang, "Switchable metamaterial reflector/absorber for different polarized electromagnetic waves," *Appl. Phys. Lett.*, vol. 97, no. 5, Aug. 2010, Art. no. 051906.
[37] B. Ratni, A. de Lustrac, G.-P. Piau, and S. N. Burokur, "Electronic control of linear-to-circular polarization conversion using a reconfigurable metasurface," *Appl. Phys. Lett.*, vol. 111, no. 21, Nov. 2017, Art. no. 214101.
[38] R. C. Yang, J. P. Xu, J. Y. Wang, R. B. Ma, and W. M. Zhang, "Frequency-reconfigurable metamaterial absorber/reflector with eight operating modes," *Opt. Express*, vol. 27, no. 12, pp. 16550–16559, Jun. 2019.
[39] Z. J. Luo, Q. Wang, X. G. Zhang, J. W. Wu, J. Y. Dai, L. Zhang, H. T. Wu, H. C. Zhang, H. F. Ma, Q. Cheng, and T. J. Cui, "Intensity-dependent metasurface with digitally reconfigurable distribution of nonlinearity," *Adv. Opt. Mater.*, vol. 27, no. 12, May 2019, Art. no. 1900792.
[40] L. Wang, W. Hong, L. Deng, S. Li, C. Zhang, J. Zhu, and H. Wang, "Reconfigurable multifunctional metasurface hybridized with vanadium dioxide at terahertz frequencies," *Materials*, vol. 11, no. 10, p. 2040, Oct. 2018.
[41] P. C. Wu, W. Zhu, Z. X. Shen, P. H. J. Chong, W. Ser, D. P. Tsai, and A.-Q. Liu, "Broadband wide-angle multifunctional polarization converter via liquid-metal-based metasurface," *Adv. Opt. Mater.*, vol. 5, no. 7, Apr. 2017, Art. no. 1600938.
[42] X. Gao, W. L. Yang, H. F. Ma, Q. Cheng, X. H. Yu, and T. J. Cui, "A reconfigurable broadband polarization converter based on an active metasurface," *IEEE Trans. Antennas Propag.*, vol. 66, no. 11, pp. 6086–6095, Nov. 2018.
[43] Y. Zhou, X. Cao, J. Gao, H. Yang, and S. Li, "Reconfigurable metasurface for multiple functions: Magnitude, polarization and phase modulation," *Opt. Express*, vol. 26, no. 22, pp. 29451–29459, Oct. 2018.
[44] Y. Li, Y. Wang, and Q. S. Cao, "Design of a multifunctional reconfigurable metasurface for polarization and propagation manipulation," *IEEE Access*, vol. 7, pp. 129183–129191, 2019.
[45] *Precision Thick Film Chip Resistors*. Accessed: Jun. 6, 2020. [Online]. Available: https://industrial.panasonic.com/cdbs/www-data/pdf/RDA0000/AOA0000C304.pdf
[46] *BA591 Band-Switching Diode*. Accessed: Jun. 6, 2020. [Online]. Available: https://www.nxp.com/docs/en/data-sheet/BA591.pdf
[47] *NRL Arch Reflectivity Testing*. Accessed: Jun. 6, 2020. [Online]. Available: http://www.eccosorb.com/Collateral/Documents/English-US/nrl_arch_reflectivity_testing.pdf

JIAYUN WANG was born in Datong, China, in 1991. He received the B.S. degree in computer science and technology from the Heilongjiang University of Science and Technology, Harbin, China, in 2014. He is currently pursuing the Ph.D. degree in electromagnetic metamaterials with Shanxi University.

RONGCAO YANG was born in Yuncheng, China, in 1970. She received the B.S. and M.S. degrees in electronics and information technology and the Ph.D. degree in optics from Shanxi University, Taiyuan, China, in 1995, 1997, and 2005, respectively. She is currently a Professor with the College of Physics and Electronics, Shanxi University. Her current research interests include electromagnetic metamaterials, nanophotonic devices, and optical communications.

RUNBO MA (Member, IEEE) was born in Shanxi, Changzhi, China, in 1974. He received the B.S., M.S., and Ph.D. degrees in electronic engineering from Shanxi University, Taiyuan, China, in 1993, 2002, and 2011, respectively. He is currently an Associate Professor with the College of Physics and Electronics, Shanxi University. His research interests include microwave and millimeter-wave integrated circuits, RFID, and microstrip antenna.

JINPING TIAN was born in 1975. He received the B.S. degree in electronics and information system and the Ph.D. degree in optics from Shanxi University, Taiyuan, China, in 1997 and 2006, respectively. He is currently a Professor with the Computer Center and the College of Physics and Electronics Engineering, Shanxi University. His current research interests include surface plasmonic waveguides and nanometer photonic devices.

WENMEI ZHANG (Member, IEEE) was born in 1969. She received the B.S. and M.S. degrees from the Nanjing University of Science and Technology, Nanjing, China, in 1992 and 1995, respectively, and the Ph.D. degree in electronic engineering from Shanghai Jiao Tong University, Shanghai, China, in 2004. She is currently a Professor with the College of Physics and Electronics, Shanxi University, Taiyuan, China. Her current research interests include microwave and millimeter-wave integrated circuits, EMC, and microstrip antenna.